Water dynamics in pristine and porous $Ti_3C_2T_x$ MXene as probed by quasielastic neutron scattering

Murillo L. Martins,[1,*] Tyler S. Mathis,[2] Xuehang Wang,[2] Luke L. Daemen,[1] Yury Gogotsi,[2] and Eugene Mamontov[1,†]

[1]*Neutron Scattering Division, Oak Ridge National Laboratory, P.O. Box 2008, MS6455, Oak Ridge, Tennessee 37831, USA*

[2]*A. J. Drexel Nanomaterials Institute and Department of Materials Science and Engineering, Drexel University, Philadelphia, Pennsylvania 19104, USA*

(Received 19 October 2021; accepted 9 February 2022; published 1 March 2022)

MXenes are a novel class of two-dimensional (2D) materials whose applications in energy-storage systems have attracted substantial attention. Still, the rate performance of these materials is often diminished by sheet restacking, which is attenuated via controlled etching in H_2SO_4 solution. With this process, micropores are formed in MXene sheets that allow transport across 2D layers. As a result, the intercalation and diffusivity of ions are facilitated resulting in improved capacitance retention at high charge-discharge rates. In the present work, we used quasielastic neutron scattering to evaluate the potential changes in water dynamics as a consequence of this mechanism by assessing the behavior of weakly and strongly confined water populations in pristine and porous MXenes. First, we have found that the porous sample accommodates a noticeably higher content of both water populations. Additionally, the fraction of mobile molecules is higher either under strong or weak confinement. Interestingly, regardless of the abundance of weakly confined water in the porous sample, no considerable changes in the dynamical behavior were detected in comparison with the dynamics measured in the pristine material. For the strongly confined populations of water, our results show that water is able to permeate the micropores introduced by etching and perform unlocalized motions.

DOI: 10.1103/PhysRevMaterials.6.034001

I. INTRODUCTION

In recent years, uncountable efforts have been dedicated to design two-dimensional (2D) materials aimed at applications in energy storage, gas sensing, and others [1,2]. Among these materials, MXenes have attracted considerable attention since they were reported in 2011 [3]. Typically, MXenes can be described by the general formula $M_{n+1}X_nT_x$ ($n = 1, 2, 3, 4$) where M stands for an early transition metal (Ti, Nb, Mo, V, Cr, Ta, etc.), X is carbon and/or nitrogen, and T_x are the surface functional groups $-$F, $=$ O, -Cl, or -OH [4]. Thanks to this compositional versatility, MXenes are among the largest families of materials ever reported and, as such, can have their chemical and physical properties tuned to attend to specific demands. For example, this class of materials has been successfully used in applications related to microwave absorption, N_2 capture, catalysis, and medicine [5–8]. Most importantly for this work, MXenes are notably promising for energy-storage applications [9,10].

In particular, titanium carbide ($Ti_3C_2T_x$) has been shown to possess a broad range of indispensable properties for charge storage purposes, such as high electronic conductivity (exceeding 20 000 S cm^{-1}) [11] and high volumetric capacitance and rate performance [4]. As commonly observed in 2D materials, the stacking of $Ti_3C_2T_x$ may be, in principle, a limitation to the design of thick electrodes, since it imposes long ion transport pathways and, consequently, low rate performance [12,13]. However, not only can the composition of MXenes be adjusted to accomplish desired properties, but also their structure and morphology. Within this context, several attempts have been made focusing on attenuating the restacking in $Ti_3C_2T_x$ films. For example, the interlayer insertion of nanomaterials (graphene, carbon nanotube, and others) has been explored [14,15]. Nevertheless, in general, the reported increases in rate performances are accompanied by a reduction of volumetric capacitance due to the presence of inactive materials, excess spacing, or active materials with lower volumetric capacitance. Within the same scope, irreversible oxidation of the $Ti_3C_2T_x$ sheets has also been tested, but a somewhat similar outcome was observed as the interlayer spacing was increased via the formation of electrochemically inactive titania nanostructures [16]. Contrarily, *in situ* anodic oxidation has shown to be a promising approach since, in this case, the increase in the interlayer spacing was concomitant to the introduction of pores in the MXene structure, which prevents the impairment of the material's rate performance [4]. With this approach, the main limitation remains in the difficulties associated with its large-scale application.

Recently, a scalable strategy to emulate the results obtained via *in situ* anodic oxidation was reported by Tang *et al.* [17] based on the partial etching of $Ti_3C_2T_x$ films with highly concentrated H_2SO_4. With this method, an increased interlayer spacing was achieved following an increase in the d spacing of 0001 planes from 12 to 13 Å together with the generation of micropores in MXene sheets and minimal formation of electrochemically inactive side products. As an outcome, the resulting MXene demonstrated ultrahigh rate performance and improved capacitance retention at high scan rates.

Different from double-layer capacitors (the so-called supercapacitors), the energy storage in MXenes has a pseudocapacitive nature in protic electrolytes, which relies on the

*longomartiml@ornl.gov
†mamontove@ornl.gov

mobility of protons intercalated between the sheets of the 2D material [18] and is certainly facilitated by the formation of micropores via etching. In recent works, the crucial participation of the electrolytes in the charge storage mechanisms in MXene has been exposed [19,20] and the interplay between solvation/desolvation of intercalated ions has shown to be decisive [21,22]. In the case of MXene etched via treatment with H_2SO_4, the mechanisms governing the diffusion of Li^+ through the newly formed micropores have not been elucidated and, most importantly, it is still not clear if water can permeate these diffusive channels and effectively participate in the charge storage mechanism.

Therefore, in this work, we focus on the dynamics of water in MXene before and after etching with H_2SO_4 solution. To characterize these confined dynamics, we resort to quasielastic neutron scattering (QENS), which is a highly suitable technique for the dynamical characterization of various H-rich systems, including water confined in MXenes [23–28]. By investigating either air-dried or annealed $Ti_3C_2T_x$ samples, before and after etching in H_2SO_4, we have been able to describe the dynamical behavior of weakly and strongly confined water. While the former can be somewhat influenced by the populations of water in the interstack spaces of MXene, the latter reflects the dynamics of molecules in the interlayer spacing and the micropores. We observed that the etched porous sample can accommodate a substantially higher content of weakly confined water but with no prejudice to the diffusivity of these molecules. As we turned to the strongly confined water molecules, these, counterintuitively, do not behave as strongly bound populations and perform rather fast motions. We also show that these molecules are also more abundant in the porous sample as a consequence of molecules permeating the micropore network introduced by the chemical treatment.

II. EXPERIMENT

A. Sample preparation

$Ti_3C_2T_x$ MXene, which is the first discovered and most studied MXene with many outstanding properties, was used in this study. Samples were prepared as described in Ref. [17]. Part of the resulting MXene powder was treated in $3M$ H_2SO_4 at ∼100 °C, washed until *p*H neutralization, and air dried at 40 °C for gradual removal of excess water. To produce pores in MXene sheets that would allow the transport of water and ions across the layers, we used a chemical etching process. $Ti_3C_2T_x$ nanosheets were mixed with diluted H_2SO_4 in solution and concentrated by evaporation in a vacuum oven at ∼60 °C overnight. The etching process took place in a single step. The washed and redispersed $Ti_3C_2T_x$ nanosheets were finally vacuum filtrated into films. For a detailed description of the etching of MXene, the readers are also referred to Ref. [17]. The pristine powder was also washed and air dried following the same procedures as used for the etched sample. These preparation steps created air-dried pristine and etched samples. Finally, separated fractions of both the etched and pristine samples were further annealed at 110 °C under vacuum for 10 h for the removal of weakly bound water. This additional treatment step created annealed pristine and etched samples.

B. X-ray powder diffraction (XRD) and N_2 sorption measurements

For the XRD experiments, a Panalytical X'pert Materials Powder Diffractometer Pro equipped with an X'Celerator solid-state detector was used. The annealed samples of etched and pristine MXene were analyzed with x rays generated at 45 kV/40 mA with a wavelength of $\lambda = 1.5418$ Å (Cu $K\alpha$ radiation). For the N_2 adsorption experiments, the annealed samples were dried for 3 h at 90 °C under vacuum (10^{-4} mbar) and the measurements were performed following the Brunauer-Emmett-Teller (BET) method with a Gemini VII (Micromeritics) instrument.

C. Quasielastic neutron scattering (QENS) measurement and analysis

Air-dried and annealed MXene powders, both etched and pristine, were investigated with QENS experiments performed on the backscattering spectrometer BASIS at Spallation Neutron Source, Oak Ridge National Laboratory, USA [29]. BASIS's energy resolution is 3.7 μeV (full width at half maximum for the Q-averaged resolution value) and its dynamic range of accessible energy transfer values is ± 100 μeV. For the experiments, the samples were placed in flat plate aluminum sample holders and positioned perpendicularly to the neutron beam. To mitigate the effects of multiple scattering [30], the samples' thickness was set as 0.25 mm. For comparison, a sample should ideally scatter about 5%–10% of the incident neutrons and a sample of dry MXene with the same thickness would yield a transmission of 98%–95% (as estimated with the tool available in Ref. [31]), depending on the density (which can be as high as 3.7 g cm^{-3} [32]).

Temperature-dependent neutron elastic scattering intensity scans were performed between 20 and 300 K with 1 K steps to provide insight into the activation of motions within the samples. Different from backscattering spectrometers with Doppler-driven monochromators located at reactor sources, in which the elastic intensity alone can be measured at zero energy transfer with the monochromator at rest, BASIS collects the data at all energy transfer values simultaneously due to the polychromatic nature of the incident beam [33]. Hence, the elastic intensity is defined as the integrated energy under the elastic line (that is, between ±3.7 μeV). Then, full QENS spectra were collected at 300 K with better statistics to allow for the analysis of dynamical features within the samples. QENS spectra were also collected at 10 K for each sample and were used as instrument resolutions in the data analysis. After collection of the data, these were reduced following routine procedures with the software MANTID [34], including normalization to a flat-plate vanadium standard, subtraction of the instrumental background using the data collected from an empty sample holder, and application of a mask file to exclude noisy detectors. No multiple scattering correction has been performed. The data analyses were performed using the fitting package QCLIMAX [35].

III. RESULTS AND DISCUSSION

In Fig. 1(a), the XRD data for the pristine and etched MXenes are presented and the results agree with those previously reported by Tang *et al.* [17] as follows. The etching

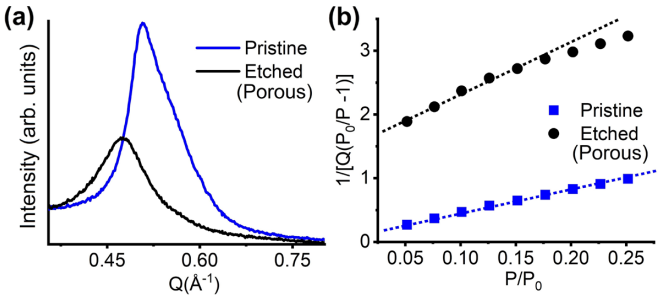

FIG. 1. (a) XRD data for pristine and etched MXene. (b) Results from N_2 sorption experiments for pristine and etched porous MXene. The linear relative pressure ranges for each sample are highlighted by the dotted lines.

of the material leads to a shift of the Bragg reflection from the 0001 planes from $Q = 0.51$ to 0.47 Å^{-1}. Hence, following $d = 2\pi/Q$, the d spacing (d) increases from ∼12 to ∼13 Å, and one can also envisage an increase in the interlayer spacing accessible for water molecules. According to Tang *et al.* [17], the slightly increased interlayer spacing in the etched $Ti_3C_2T_x$ MXene can be attributed to two factors: (i) the presence of residual sulfur compounds that were not washed from the samples after treatment in H_2SO_4 and that remain physically or chemically adsorbed on the material's surfaces, and (ii) the *in situ* formation of carbon species on the surfaces of MXene in the regions where Ti atoms are partially oxidized and removed by the etching process. Also, one should notice that Tang *et al.* [17] performed the XRD experiments with air-dried samples while we have used annealed materials. The similarities between our results, therefore, indicate that the annealing of the samples does not disrupt the core structure of the MXenes. Clearly, the Bragg reflection from the etched sample is broader, which can be associated with a better dispersion of the MXene stacks during the washing procedure. In Fig. 1(b), the results obtained from the N_2 sorption measurements are presented and BET-specific surface areas were tentatively calculated using the Brunauer-Emmett-Teller equation in the linear region of the relative pressure between 0.05 and 0.25. For the pristine sample, the BET surface area has been determined as $26\,m^2/g$, which is also in agreement with values reported elsewhere [18]. After etching, the linear range of the BET plot shifts to relative pressures below 0.15 (as highlighted by the dotted line in the figure) indicating that the chemical treatment was gentle and micropores were predominantly introduced in the material with dimensions not assessed by the N_2 molecules (one should notice that the kinetic diameter of N_2 is ∼37% higher than of water [36,37]).

Turning to the QENS results, in Fig. 2, the temperature-dependent neutron elastic scattering intensity scans are presented. For better statistics, the scans are presented as sums of the data collected between $Q = 0.3$ and 1.1 Å^{-1}. In Fig. 2(a), the data are normalized by the samples' masses and a Q-independent perception of the absolute intensities of the elastic scattering is possible. In the air-dried samples, the absolute values of the elastic intensities are around 90% higher in the porous MXene as compared with the pristine material, indicating that the chemical treatment leads to a remarkably higher content of water and H-rich surface groups.

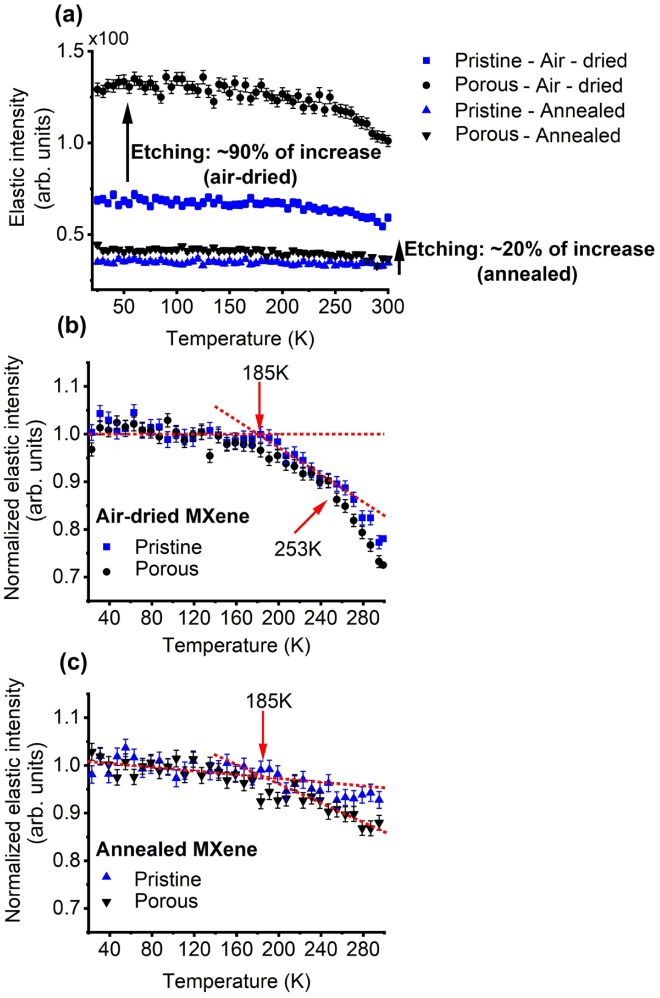

FIG. 2. Temperature-dependent neutron elastic scattering intensity scans for pristine and porous MXene powders before (air-dried) and after annealing. The results are presented as the sums of the data collected between $Q = 0.3$ and 1.1 Å^{-1}. In (a), the data were normalized by the samples' masses. In (b,c) the data collected at 20 K were normalized to unit. In (b,c) the red lines are guides for the eye.

After annealing and the elimination of weakly confined water molecules, the QENS signals drop around 60%–70% in both samples at the lowest temperatures (that is, before any dynamic events are activated in the samples). Still, the absolute values of the elastic intensities are around 20% higher in the porous sample as compared with the pristine MXene.

Figures 2(b) and 2(c) show the temperature-dependent neutron elastic scattering intensity scans normalized by the value of the data points collected at 20 K. With this representation, one can observe the behavior of the fraction of immobile species within each sample, the so-called elastic scattering fractions, at the experimental temperatures, and, most importantly, the activation of dynamic processes within the samples. In the air-dried samples, Fig. 2(b), the lack of freezing-melting transition, as indicated by the absence of abrupt drops in the elastic intensity, confirms that the dynamics assessed by the experiments is predominantly from confinedlike populations of water. In these materials, the activation of the dynamic

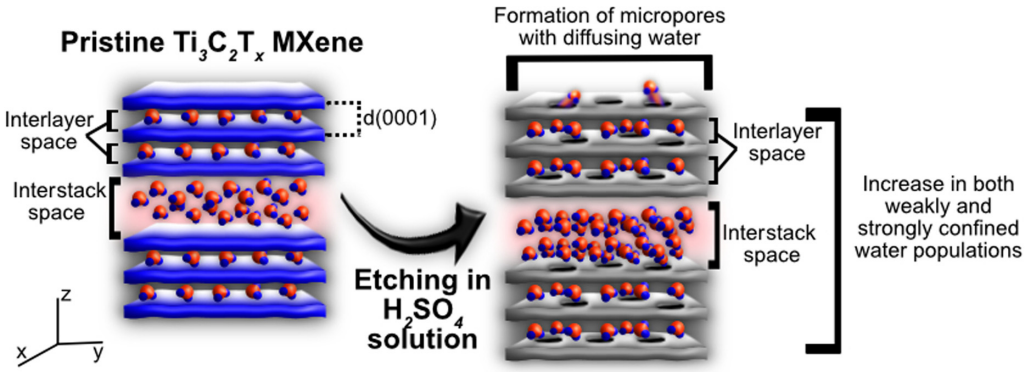

FIG. 3. Representation of the changes caused in MXene by treatment in H_2SO_4 solution and distribution of water populations in interlayer and interstack spaces. After etching, micropores are formed in the MXene sheets and the interlayer space subtly increases due to the presence of sulfur- and carbon-based compounds as discussed in Ref. [17]. After etching, micropores are formed in the sheets of $Ti_3C_2T_x$ MXene. Overall, the porous material retains a larger content of weakly and strongly confined water as compared with the pristine material.

motions occurs at two steps as indicated in the figure: around 185 and 253 K [the red lines in Figs. 2(b) and 2(c) are guides for the eye]. Regarding the fraction of scatters that are immobilized (or slower than the characteristic time corresponding to the instrument energy resolution, that is, whose motions' timescale is longer than ∼0.36 ns), these seem to be more abundant in the pristine sample, as demonstrated by the relatively higher elastic intensity around room temperature. This feature will be discussed further in the paper based on the analysis of the QENS full spectra collected at 300 K. After annealing the powders, Fig. 2(c), the activation of dynamic motions around 253 K is no longer observable and a single smooth deviation in the monotonical behavior of the elastic scattering intensity scans is detected around 185 K. Here, the fraction of immobile species is also seemingly higher in the pristine sample and will be also discussed further in the paper.

In general, MXenes can accommodate water molecules in the so-called interstack and interlayer spaces as discussed in previous investigations with QENS [19] and represented in Fig. 3. In this figure, the subtle increase in interlayer spacing, as well as the formation of micropores in the etched material, as indicated by the results in Fig. 1, are also represented. Intuitively, the molecules in the interstack region are expected to be more abundant and subjected to weaker confinement, whereas strongly confined molecules are found in the interlayer spaces. Thus, since the water population activated at ∼253 K is eliminated upon annealing, it is reasonable to assume that molecules in the interstack region contribute, at least to a certain extent, to this relaxation. Following the same rationale, we may infer that, in the motions activated at ∼185 K, the contributions from the interstack water are scarcer and the dynamics are dominated by the molecules trapped within the interlayer spaces or in the micropores conceived by the etching process. Controversially, however, the lower temperature of dynamic activation suggests that, although these populations are subjected to a stricter confinement geometry, they are not necessarily strongly bound to the surfaces of MXene.

A deeper understanding of the dynamical processes revealed by the elastic scattering intensity scans is provided by the analysis of the full QENS spectra collected at 300 K. Typically, the measured intensity of the QENS experiments, $I(Q, E)$, can be described as follows:

$$I(Q,E) = \{x(Q)\delta(E) + [1 - x(Q)]S(Q,E) + B(Q,E)\} \otimes R(Q,E), \quad (1)$$

where $x(Q)$ is the elastic fraction of the signal; $\delta(E)$ is a Dirac delta function accounting for the referred elastic scattering (zero energy transfer); $S(Q, E)$ is the dynamic structure factor, i.e., the QENS model scattering function; B(Q, E) is a linear background; and $R(Q, E)$ corresponds to the instrument resolution function (here the data collected at 10 K for each sample). In our analyses, $B(Q, E)$ accounts for dynamical processes that are too fast for the dynamic range of the instrument (that is, with timescales shorter than a few picoseconds) and, possibly, sample- and temperature-dependent backgrounds. Here, $S(Q, E)$ is described by a single Lorentzian function:

$$S(Q,E) = \frac{1}{\pi}\left[\frac{\Gamma(Q)}{\Gamma^2(Q) + E^2}\right], \quad (2)$$

where $\Gamma(Q)$ is the half width at the half maximum of the curve. In other words, in the (Q, t) domain, the QENS signal (or the so-called intermediate scattering function) would be perceived as a probability function exponentially decaying over time. With these considerations, the experimental data collected at 300 K were fitted with Eq. (1).

Let us first discuss qualitatively the full QENS spectra and some outcomes obtained by fitting the data. In Figs. 4(a) and 4(b), the QENS spectra collected at $Q = 1.1$ Å^{-1} for the air-dried pristine and porous samples are displayed as representative results. In the figures, the resolution and the Lorentzian $S(Q, E)$ functions are also shown together with the total fit of the data. Visually, one can observe that the contribution of $S(Q, E)$ in the porous material is larger than in the pristine. However, as shown in Fig. 4(c), where the intensities of $S(Q, E)$ are normalized to unity, the broadenings of the curves are nearly the same, indicating that the dynamic motions are more abundant in the porous material but similar in characteristic time to those detected in the pristine MXene. In Figs. 4(d) and 4(e), the results from the annealed samples are presented and the larger contribution of $S(Q, E)$ in the porous

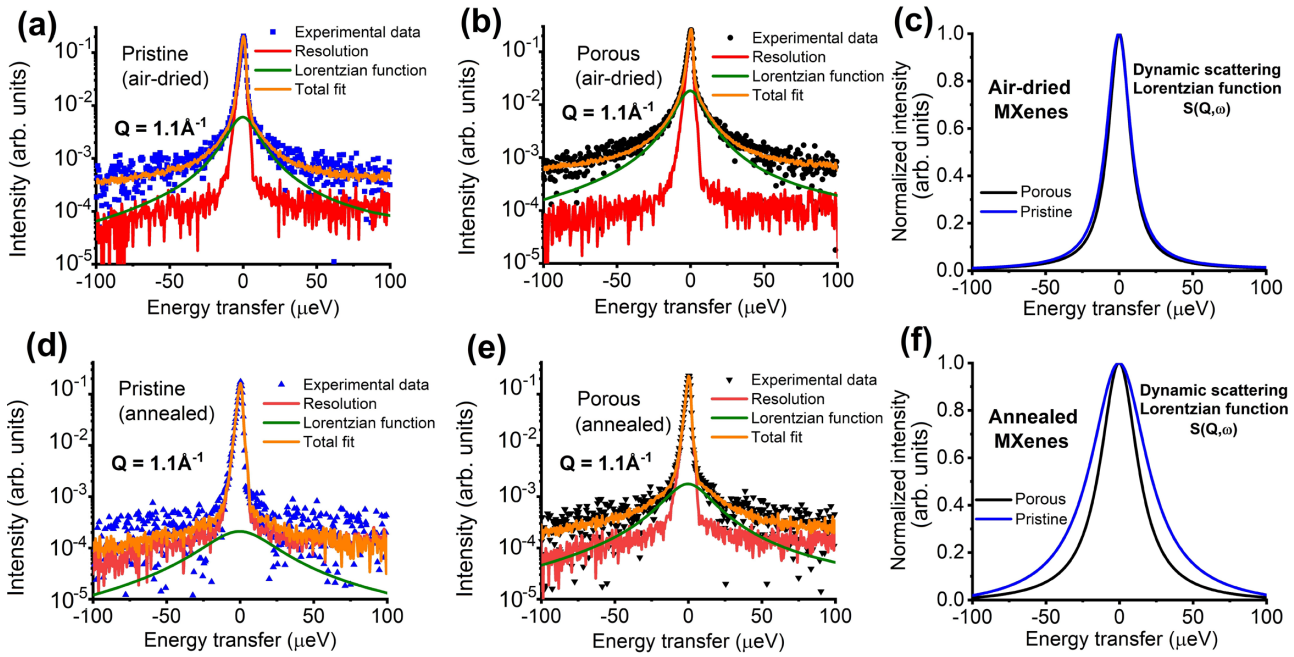

FIG. 4. Representative QENS spectra collected at 300 K and $Q = 1.1$ Å^{-1} for the air-dried (a) pristine and (b) etched porous samples. The resolution and the Lorentzian $S(Q, E)$ functions are also shown (red and green lines) together with a fit of the data obtained with Eq. (1) (orange lines). (c) Normalized $S(Q, E)$ for the air-dried pristine and porous samples as determined by fitting the data with Eq. (1). In (d), (e), the QENS spectra collected at 300 K and $Q = 1.1$ Å^{-1} for the annealed pristine and porous samples are shown, respectivelly. (f) Normalized $S(Q, E)$ for the annealed pristine and porous samples as also determined by fitting the data with Eq. (1). The intensities in (c), (f) are in linear scale while the others are in log scale.

material is also visually observable. In this case, as shown in Fig. 4(f), the dynamic motions detected in the porous sample are notably slower than in the pristine MXene, as depicted by the difference in the broadening of the curves. Interestingly, while comparing the plots in Fig. 4(f) with those in Fig. 4(c), the dynamics found in the annealed samples are faster than those in the air-dried MXene. This observation sustains the hypothesis that the annealed samples hold water molecules that are subjected to stricter confinement geometries but are not necessarily strongly bound to the MXene surfaces.

Turning to a quantitative analysis of the results obtained by fitting the QENS spectra with Eq. (1), Fig. 5(a) shows the values of $x(Q)$ for the different samples whose values at high Q indicate the fraction of scatters that are immobile or slower than the instrument resolution. Due to divergence in the fitting process caused by the very subtle differences between the contributions from $x(Q)$ and S(Q, E) in the annealed pristine sample, the data were initially fitted solely with an elastic contribution. Then, the elastic contribution was fixed, and the dynamic scattering function was included in the model. In the end, the elastic contribution was slowly adjusted until the best agreement between the experimental data and the model was achieved. Because of this procedure, no error bars are shown for $x(Q)$ in this sample. Here, these results complement the observations made based on Fig. 2 and show that the porous material, either before or after annealing, not only accommodates higher contents of water but also allows for a higher fraction of these molecules to engage in dynamic motions.

Sequentially, the Q dependence of $\Gamma(Q)$ was evaluated. For the air-dried samples, given the higher density of scattering centers under analysis and the consequently less continuous media [38], microscopic mechanisms are relevant at large Q values, that is, distances smaller than several molecular diameters. Therefore, the values of $\Gamma(Q)$ follow a Q dependence well described by an unrestricted diffusion law with an exponential distribution of the diffusion jump lengths [39]:

$$\Gamma(Q) = \frac{\hbar D Q^2}{1 + D Q^2 \tau_0}, \tag{3}$$

where $\hbar = 6.5821 \times 10^{-16}$ μeV s, τ_0 is the residence time between jumps between two sites, and D is the diffusion coefficient. As depicted in Fig. 5(b), there are no considerable dynamical differences between the air-dried samples [as also suggested in Fig. 4(c)]. In other words, even though etching allows for a larger content of weakly confined populations of water, the chemical environment is likely similar to the pristine material. Here, the determined diffusivities, $D_{\text{pristine}} = 2.51 \pm 0.35 \times 10^{-10}$ m^2/s and $D_{\text{etched}} = 2.28 \pm 0.1 \times 10^{-10}$ m^2/s for the pristine and porous samples, are lower than the diffusivity determined by Osti *et al.* [26] for interstack motions of water in MXene ($\sim 11 \times 10^{-10}$ m^2/s). In the present work, the reported diffusivities are more comparable to the value estimated by Osti *et al.* for a single layer of water between MXene layers (5.33×10^{-10} m^2/s) and much higher than the values estimated for interlayer water diffusing in ion-intercalated MXenes (0.28×10^{-10} m^2/s). Hence, from these comparisons, the contributions from interstack water in the motions detected in the air-dried samples are likely to be present but are not dominant.

Turning to the analysis of the annealed samples, as also shown in Fig. 5(b), the values of $\Gamma(Q)$ follow a Q dependence

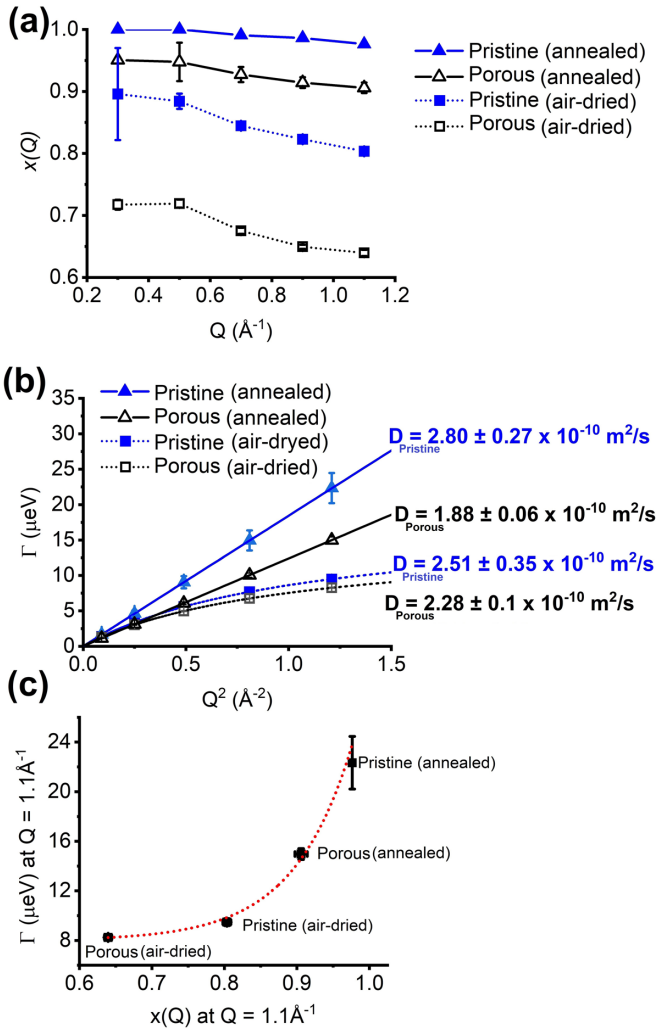

FIG. 5. (a) Q dependence of the elastic fraction $x(Q)$ as obtained by fitting the QENS data with Eqs. (1) and (2). As explained in the text, $x(Q)$ has been fixed during the fits for the annealed pristine sample and no error bars are shown. (b) Q dependence of the broadening, $\Gamma(Q)$, of the QENS signals from annealed samples of pristine and porous MXenes. The lines represent the fits with either Eq. (3) (jump diffusion), or the $\hbar DQ^2$ law, and the diffusivities and relaxation times (if obtained) of each sample are also shown. (c) Relationship between $\Gamma(Q)$ and $x(Q)$ at $Q = 1.1$ Å^{-1}. The dotted line is a guide for the eye.

that can be described by the $\hbar DQ^2$ law of continuous diffusion, which corresponds to the limiting case of Eq. (3) with $\tau_0 = 0$. In these cases, the underlying microscopic mechanisms that could lead to a plateau in the values of $\Gamma(Q)$ at high Q, as predicted by Eq. (3), are no longer detected in the experiments. Similar outcomes have been observed elsewhere with QENS investigations on confined water [40–42] and, in practice, do not influence the discussions of the self-diffusion coefficients since these are determined based on the data at low Q. Also, as strongly confined water molecules are under analysis, one could expect a deviation from this behavior as a plateau in the values of $\Gamma(Q)$ at the lower values of Q. Namely, for an effective confinement radius "a," $\Gamma(Q)$ would assume a nearly constant value of $4.33\,\mathrm{D}/a^2$ for $Q < 3.33/a$ [35,39,43]. The absence of such an effect in the data (Fig. 4) is due either to the influence of scattering from MXene itself at low Q values or to confinement radii large enough to lead to $Qa > 3.33$ even for $Q = 0.3$ Å^{-1}; hence $a > 11$ Å (which is the case here, considering the unconstrained geometry in the MXene's $x - y$ plane [4,17]).

Still, regarding the annealed samples, Fig. 5(b), the mobile fraction of the remaining water molecules experiences a reduction in the diffusivity after etching ($D_{\mathrm{pristine}} = 2.80 \pm 0.27$ vs $D_{\mathrm{etched}} = 1.88 \pm 0.06 \times 10^{-10}$ m^2/s. Here, the lower diffusivity of water in the etched material, despite the higher content of mobile molecules, confirms that water permeates the newly formed micropore network and performs slow, unlocalized motions not allowed in the pristine material. This result is in line with a previous report on the presence and mobility of molecular hydrogen in etched MXene [44]. Contrarily, in the pristine material, given the absence of the surface modifications promoted by the chemical treatment, a portion of the water molecules is more easily immobilized by the interfaces of MXene and only contributes to the elastic fraction of the QENS signal, $x(Q)$.

The relationship between the water dynamics in the air-dried and annealed samples and $x(Q)$ is summarized by the plot in Fig. 5(c) where the broadening of the QENS signal, $\Gamma(Q)$, is presented as a function of $x(Q)$ (the red line is a guide for the eye). Overall, the etched material accommodates a larger content of mobile water, either under strong or weak confinement (that is, in the annealed or air-dried sample, respectively). For the weakly confined, however, there are little to no changes in the chemical environment of the water molecules, which ultimately leads to very comparable diffusivities and broadening of the QENS signals. This is not the case for the strongly confined water populations as these diffuse through very distinct paths in the etched material as compared with the pristine one.

IV. CONCLUSIONS

The dynamics of water in pristine and acid-etched porous $Ti_3C_2T_x$ MXenes was investigated with air-dried and annealed samples using QENS experiments. In the air-dried samples, weakly and strongly confined water molecules contribute to the QENS signal while in the annealed materials the strongly confined populations are the sole contributors to the collected data. Then, the presence of interstack water is minimal in the annealed MXene and we can assess the dynamics in the interlayer spaces and within the micropores introduced via etching. Our results show that the etched MXene accommodates a significantly higher content of strongly and weakly confined water and holds a larger fraction of molecules that perform motions beyond the instrumental resolution. Ultimately, our results show that the strongly confined populations of water permeate the micropores formed via etching and can still perform unlocalized motions. Also, despite the richness of weakly confined water in the etched MXene, no changes in the dynamical behavior of this water population were detected in comparison with the pristine material, indicating that the diffusive paths are more abundant but preserve a similar chemical environment.

ACKNOWLEDGMENTS

This research used resources at the Spallation Neutron Source, a DOE Office of Science User Facility operated by the Oak Ridge National Laboratory. This work was supported as part of the Fluid Interface Reactions, Structures and Transport (FIRST) Center, an Energy Frontier Research Center funded by the U.S. Department of Energy, Office of Science, Office of Basic Energy Sciences. This research used resources of the National Energy Research Scientific Computing Center, a DOE Office of Science User Facility supported by the Office of Science of the U.S. Department of Energy under Contract No. DE-AC0205CH11231. Oak Ridge National Laboratory is managed by UT-Battelle, LLC, for U.S. DOE under Contract No. DEAC05-00OR22725. The authors are also thankful to Dr. Jong K. Keum for support with the XRD analyses.

[1] B. Liu, and K. Zhou, Recent progress on graphene-analogous 2D nanomaterials: Properties, modeling and applications, Prog. Mater. Sci. **100**, 99 (2019).

[2] N. R. Glavin, R. Rao, V. Varshney, E. Bianco, A. Apte, A. Roy, E. Ringe, and P. M. Ajayan, Emerging applications of elemental 2D materials, Adv. Mater. **32**, 1904302 (2020).

[3] M. Naguib, M. Kurtoglu, V. Presser, J. Lu, J. Niu, M. Heon, L. Hultman, Y. Gogotsi, and M. W. Barsoum, Two-dimensional nanocrystals produced by exfoliation of Ti_3AlC_2, Adv. Mater. **23**, 4248 (2011).

[4] J. Tang, T. S. Mathis, N. Kurra, A. Sarycheva, X. Xiao, M. N. Hedhili, Q. Jiang, H. N. Alshareef, B. Xu, F. Pan, and Y. Gogotsi, Tuning the electrochemical performance of titanium carbide mxene by controllable *in situ* anodic oxidation, Angew. Chem., Int. Ed. **58**, 17849 (2019).

[5] M. S. Cao, Y. Z. Cai, P. He, J. C. Shu, W. Q. Cao, and J. Yuan, 2D MXenes: Electromagnetic property for microwave absorption and electromagnetic interference shielding, Chem. Eng. J. **359**, 1265 (2019).

[6] L. M. Azofra, N. Li, D. R. MacFarlane, and C. Sun, Promising prospects for 2D d^2-d^4 M_3C_2 transition metal carbides (MXenes) in N_2 capture and conversion into ammonia, Energy Environ. Sci. **9**, 2545 (2016).

[7] J. Zhu, E. Ha, G. Zhao, Y. Zhou, D. Huang, G. Yue, L. Hu, N. Sun, Y. Wang, L. Y. S. Lee, C. Xu, K. Y. Wong, D. Astruc, and P. Zhao, Recent advance in MXenes: A promising 2D material for catalysis, sensor and chemical adsorption, Coord. Chem. Rev. **352**, 306 (2017).

[8] H. Lin, S. Gao, C. Dai, Y. Chen, and J. Shi, A two-dimensional biodegradable niobium carbide (MXene) for photothermal tumor eradication in NIR-I and NIR-II biowindows, J. Am. Chem. Soc. **139**, 16235 (2017).

[9] J. C. Lei, X. Zhang, and Z. Zhou, Recent advances in MXene: preparation, properties, and applications, Front. Phys. **10**, 276 (2015).

[10] B. Anasori, M. R. Lukatskaya, and Y. Gogotsi, 2D metal carbides and nitrides (MXenes) for energy storage, Nat. Rev. Mater. **2**, 16098 (2017).

[11] T. S. Mathis, K. Maleski, A. Goad, A. Sarycheva, M. Anayee, A. C. Foucher, K. Hantanasirisakul, C. E. Shuck, E. A. Stach, and Y. Gogotsi, Modified MAX phase synthesis for environmentally stable and highly conductive Ti_3C_2 MXene, ACS Nano **15**, 6420 (2021).

[12] M. R. Lukatskaya, S. Kota, Z. Lin, M.-Q. Zhao, N. Shpigel, M. D. Levi, J. Halim, P.-L. Taberna, M. W. Barsoum, P. Simon, and Y. Gogotsi, Ultra-high-rate pseudocapacitive energy storage in two-dimensional transition metal carbides, Nat. Energy **2**, 17105 (2017).

[13] J. D. Gouveia, F. Viñes, F. Illas, and J. R. B. Gomes, MXenes atomic layer stacking phase transitions and their chemical activity consequences, Phys. Rev. Materials **4**, 054003 (2020).

[14] M.-Q. Zhao, C. E. Ren, Z. Ling, M. R. Lukatskaya, C. Zhang, K. L. Van Aken, M. W. Barsoum, and Y. Gogotsi, Flexible MXene/carbon nanotube composite paper with high volumetric capacitance, Adv. Mater. **27**, 339 (2015).

[15] J. Yan, C. E. Ren, K. Maleski, C. B. Hatter, B. Anasori, P. Urbankowski, A. Sarycheva, and Y. Gogotsi, Flexible MXene/graphene films for ultrafast supercapacitors with outstanding volumetric capacitance, Adv. Funct. Mater. **27**, 1701264 (2017).

[16] C. Yang, Y. Liu, X. Sun, Y. Zhang, L. Hou, Q. Zhang, and C. Yuan, *In-situ* construction of hierarchical accordion-like TiO_2/Ti_3C_2 nanohybrid as anode material for lithium and sodium ion batteries, Electrochim. Acta **271**, 165 (2018).

[17] J. Tang, T. Mathis, X. Zhong, X. Xiao, H. Wang, M. Anayee, F. Pan, B. Xu, and Y. Gogotsi, Optimizing ion pathway in titanium carbide mxene for practical high-rate supercapacitor, Adv. Energy Mater. **11**, 2003025 (2021).

[18] P. Srimuk, F. Kaasik, B. Krüner, A. Tolosa, S. Fleischmann, N. Jäckel, M. C. Tekeli, M. Aslan, M. E. Suss, and V. Presser, MXene as a novel intercalation-type pseudocapacitive cathode and anode for capacitive deionization, J. Mater. Chem. A **4**, 18265 (2016).

[19] X. Wang, T. S. Mathis, K. Li, Z. Lin, L. Vlcek, T. Torita, N. C. Osti, C. Hatter, P. Urbankowski, A. Sarycheva, M. Tyagi, E. Mamontov, P. Simon, and Y. Gogotsi, Influences from solvents on charge storage in titanium carbide mxenes, Nat. Energy **4**, 241 (2019).

[20] N. Shpigel, M. D. Levi, S. Sigalov, T. S. Mathis, Y. Gogotsi, and D. Aurbach, Direct assessment of nanoconfined water in 2D Ti_3C_2 electrode interspaces by a surface acoustic technique, J. Am. Chem. Soc. **140**, 8910 (2018).

[21] Q. Gao, W. Sun, P. Ilani-Kashkouli, A. Tselev, P. R. C. Kent, N. Kabengi, M. Naguib, M. Alhabeb, W.-Y. Tsai, A. P. Baddorf, J. Huang, S. Jesse, Y. Gogotsi, and N. Balke, Tracking ion intercalation into layered Ti_3C_2 MXene films across length scales, Energy Environ. Sci. **13**, 2549 (2020).

[22] X. Wang, T. S. Mathis, Y. Sun, W.-Y. Tsai, N. Shpigel, H. Shao, D. Zhang, K. Hantanasirisakul, F. Malchik, N. Balke, D. Jiang, P. Simon, and Y. Gogotsi, Titanium carbide MXene shows an electrochemical anomaly in water-in-salt electrolytes, ACS Nano **15**, 15274 (2021).

[23] M. L. Martins, R. Ignazzi, J. Eckert, B. Watts, R. Kaneno, W. F. Zambuzzi, L. Daemen, M. J. Saeki, and H. N. Bordallo, Restricted mobility of specific functional groups reduces anticancer drug activity in healthy cells, Sci. Rep. **6**, 22478 (2016).

[24] M. L. Martins, A. B. Dinitzen, E. Mamontov, S. Rudić, J. E. M. Pereira, R. Hartmann-Petersen, K. W. Herwig, and H. N. Bordallo, Water dynamics in MCF-7 breast cancer cells: A neutron scattering descriptive study, Sci. Rep. **9**, 8704 (2019).

[25] M. L. Martins, J. Eckert, H. Jacobsen, É. C. dos Santos, R. Ignazzi, D. R. de Araujo, M.-C. Bellissent-Funel, F. Natali, M. M. Koza, A. Matic, E. de Paula, and H. N. Bordallo, Probing the dynamics of complexed local anesthetics via neutron scattering spectroscopy and DFT Calculations, Int. J. Pharm. **524**, 397 (2017).

[26] N. C. Osti, M. Naguib, A. Ostadhossein, Y. Xie, P. R. C. Kent, B. Dyatkin, G. Rother, W. T. Heller, A. C. T. van Duin, Y. Gogotsi, and E. Mamontov, Effect of metal ion intercalation on the structure of MXene and water dynamics on its internal surfaces, ACS Appl. Mater. Interfaces **8**, 8859 (2016).

[27] M. L. Martins, A. Orecchini, L. Aguilera, J. Eckert, J. Embs, A. Matic, M. J. Saeki, and H. N. Bordallo, Encapsulation of paclitaxel into a bio-nanocomposite. A study combining inelastic neutron scattering to thermal analysis and infrared spectroscopy, EPJ Web Conf. **83**, 02011 (2015).

[28] M. L. Martins, R. L. Sacci, N. C. Sanders, J. L. Tyler, R. Matsumoto, I. Popov, W. Guo, S. Dai, P. T. Cummings, A. P. Sokolov, and E. Mamontov, addition of chloroform in a solvent-in-salt electrolyte: Outcomes in the microscopic dynamics in bulk and confinement, J. Phys. Chem. C **124**, 22366 (2020).

[29] E. Mamontov and K. W. Herwig, A time-of-flight backscattering spectrometer at the Spallation Neutron Source, BASIS, Rev. Sci. Instrum. **82**, 085109 (2011).

[30] V. F. Sears, Slow-neutron multiple scattering, Adv. Phys. **24**, 1 (1975).

[31] NIST, Neutron Activation and Scattering Calculator, https://www.ncnr.nist.gov/resources/activation/.

[32] M. Ghidiu, M. R. Lukatskaya, M.-Q. Zhao, Y. Gogotsi, and M. W. Barsoum, Conductive two-dimensional titanium carbide 'clay' with high volumetric capacitance, Nature (London) **516**, 78 (2014).

[33] E. Mamontov, H. Luo, and S. Dai, Proton dynamics in N, N, N′, N′-tetramethylguanidinium bis(perfluoroethylsulfonyl)imide protic ionic liquid probed by quasielastic neutron scattering, J. Phys. Chem. B **113**, 159 (2009).

[34] O. Arnold, J. C. Bilheux, J. M. Borreguero, A. Buts, S. I. Campbell, L. Chapon, M. Doucet, N. Draper, R. Ferraz Leal, M. A. Gigg, V. E. Lynch, A. Markvardsen, D. J. Mikkelson, R. L. Mikkelson, R. Miller, K. Palmen, P. Parker, G. Passos, T. G. Perring *et al.*, MANTID—data analysis and visualization package for neutron scattering and μSR experiments, Nucl. Instrum. Methods Phys. Res., Sect. A **764**, 156 (2014).

[35] E. Mamontov, R. W. Smith, J. J. Billings, and A. J. Ramirez-Cuesta, Simple analytical model for fitting QENS data from liquids, Physica B (Amsterdam, Neth.) **566**, 50 (2019).

[36] G. Aguilar-Armenta, M. E. Patiño-Iglesias, and R. Leyva-Ramos, Adsorption kinetic behaviour of pure CO_2, N_2 and CH_4 in natural clinoptilolite at different temperatures, Adsorpt. Sci. Technol. **21**, 81 (2003).

[37] J. E. ten Elshof, C. R. Abadal, J. Sekulić, S. R. Chowdhury, and D. H. A. Blank, Transport mechanisms of water and organic solvents through microporous silica in the pervaporation of binary liquids, Microporous Mesoporous Mater. **65**, 197 (2003).

[38] M. Bée, Localized and long-range diffusion in condensed matter: State of the art of QENS studies and future prospects, Chem. Phys. **292**, 121 (2003).

[39] M.-C. Bellissent-Funel, S. H. Chen, and J.-M. Zanotti, Single-particle dynamics of water molecules in confined space, Phys. Rev. E **51**, 4558 (1995).

[40] G. L. Jackson, S. A. Kim, A. Jayaraman, S. O. Diallo, and M. K. Mahanthappa, Consequences of convex nanopore chemistry on confined water dynamics, J. Phys. Chem. B **124**, 1495 (2020).

[41] N. C. Osti, B. P. Thapaliya, S. Dai, M. Tyagi, and E. Mamontov, Strong enhancement of nanoconfined water mobility by a structure breaking salt, J. Phys. Chem. Lett. **12**, 4038 (2021).

[42] Z. N. Buck, J. Torres, A. Miskowiec, E. Mamontov, H. Kaiser, F. Y. Hansen, H. Taub, M. Tyagi, L. Collins, and K. W. Herwig, Effect of melittin on water diffusion and membrane structure in DMPC lipid bilayers, Europhys. Lett. **123**, 18002 (2018).

[43] C. A. Bridges, M. L. Martins, C. J. Jafta, X. G. Sun, M. P. Paranthaman, J. Liu, S. Dai, and E. Mamontov, Dynamics of $Emim^+$ in [Emim][TFSI]/LiTFSI solutions as bulk and under confinement in a quasi-liquid solid electrolyte, J. Phys. Chem. B **125**, 5443 (2021).

[44] N. C. Osti, M. Naguib, M. Tyagi, Y. Gogotsi, A. I. Kolesnikov, and E. Mamontov, Evidence of molecular hydrogen trapped in two-dimensional layered titanium carbide-based MXene, Phys. Rev. Materials **1**, 024004 (2017).